

Importance of electronic correlations in exploring the exotic phase diagram of layered Li_xMnO_2

Hrishit Banerjee^{1,2,3,*}, Clare P. Grey^{1,3} and Andrew J. Morris^{2,3,†}

¹*Yusuf Hamied Department of Chemistry, University of Cambridge, Lensfield Road, Cambridge CB2 1EW, United Kingdom*

²*School of Metallurgy and Materials, University of Birmingham, Edgbaston, Birmingham B15 2TT, United Kingdom*

³*The Faraday Institution, Quad One, Becquerel Avenue, Harwell Campus, Didcot OX11 0RA, United Kingdom*



(Received 12 October 2022; revised 29 May 2023; accepted 27 September 2023; published 17 October 2023)

Using *ab initio* dynamical mean-field theory we explore the electronic and magnetic states of layered Li_xMnO_2 as a function of x , the state-of-charge. Constructing real-space Wannier projections of Kohn-Sham orbitals based on the low-energy subspace of Mn $3d$ states and solving a multi-impurity problem, our approach focuses on local correlations at Mn sites. The antiferromagnetic insulating state in LiMnO_2 has a moderate Néel temperature of $T_N = 296$ K in agreement with experimental studies. Upon delithiation the system proceeds through a number of states: ferrimagnetic correlated metals at $x = 0.92, 0.83$; multiple charge disproportionated ferromagnetic correlated metals with large quasiparticle peaks at $x = 0.67, 0.50, 0.33$; ferromagnetic metals with small quasiparticle peaks at $x = 0.17, 0.08$ and an antiferromagnetic insulator for the fully delithiated state, $x = 0.0$. At moderate states of charge, $x = 0.67 - 0.33$, a mix of $+3/+4$ formal oxidation states of Mn is observed, while the overall nominal oxidation of Mn state changes from $+3$ in LiMnO_2 to $+4$ in MnO_2 . In all these cases the high-spin state emerges as the most likely state in our calculations considering the full d manifold of Mn based on the proximity of e_g levels in energy to t_{2g} . We observe a crossover from coherent to incoherent behavior on delithiation as function of state-of-charge.

DOI: [10.1103/PhysRevB.108.165124](https://doi.org/10.1103/PhysRevB.108.165124)

I. INTRODUCTION

LiMnO_2 (LMO) [1–3] has the potential to be a low-cost, low-toxicity, high-safety, and environmentally friendly alternative to the most popular rechargeable lithium-ion battery cathode material LiCoO_2 [1,4–8]; however, at 50% delithiation LMO irreversibly transforms to a spinel ($\text{Fd}\bar{3}\text{m}$) phase, which causes significant reduction in the capacity and operating voltage, limiting its large-scale application [9–11].

The thermodynamically stable phase of LMO at ambient conditions is orthorhombic (Pmmn) [12] although a rhombohedral layered O3 structure, may be produced by ion exchange from NaMnO_2 [1,2]. The rhombohedral O3 structures comprise a family of materials, including LiCoO_2 (LCO), LiNiO_2 (LNO) [13–15], and $\text{LiNi}_{1-x-y}\text{Mn}_y\text{Co}_x\text{O}_2$ (NMC) [8,16–21]. Within this family LMO adopts the same oxygen stacking as LCO, but with symmetry reduced from rhombohedral ($\text{R}\bar{3}\text{m}$) to monoclinic (C2/m), as a result of a cooperative Jahn-Teller (JT) distortion. Based on magnetization data [12,22] pristine monoclinic LMO is an antiferromagnetic insulator in its high-spin state with relatively moderate Néel temperatures

($T_N \sim 250$ K) due to the stabilization of antiferromagnetism by the cooperative JT distortions [22].

Structural phase transitions during cycling have prevented the widespread adoption of layered monoclinic LMO as a cathode material. Upon 50% delithiation, layered phase to spinel structural phase transformation of LMO involves the migration of Mn ions, whilst the close-packed O lattice remains intact. Density functional theory (DFT) calculations, combined with a hybrid eigenvector-following method to uncover the pathways, show that for the case of $x = 0.5$, particular orderings of Li^+/Li^+ vacancy and $\text{Mn}^{3+}/\text{Mn}^{4+}$ ions play a significant role in this structural transformation [1,9,23–26]. Moreover, the ionic pathways that give rise to the ordering and transformations are highly dependent on the inclusion of a Hubbard U term in the Kohn-Sham Hamiltonian, hinting that these structural changes may have a strong underlying electronic origin. However, the role of electron correlations in the origin of the mixed-valence charge-ordered state, as well as the possibility of existence of such states at other states-of-charge remains unknown.

Electronic phase transitions occurring during cathode cycling [27–32] significantly influence the reversibility of the (de)lithiation process, in terms of rate limiting formation and propagation of phase boundaries, lattice mismatch, and volume changes, all of which lead to slow (de)lithiation kinetics hence affecting rate capability and stability, causing degradation of the active material [33]. For example, a first-order metal-insulator transition, normally driven through doping [34,35] or pressure [36,37], is driven electronically in Li_xCoO_2 as a function of states-of-charge x [30–32]. Naturally the question arises whether such an electrochemi-

*hb595@cam.ac.uk

†a.j.morris.1@bham.ac.uk

cally driven metal-insulator transition, or other exotic phases may also be observed in the analogous cathode material LMO.

Electrochemical and magnetic phase transition studies of complex layered oxides are made all the more robust through first-principles modeling of the electronic and magnetic states of these materials. Whilst the first-order metal-insulator transition observed in LCO has been postulated to be a Mott transition by some DFT studies [31,38], a true Mott transition is difficult to capture within noninteracting DFT and warrants the use of many-body methods like dynamical mean-field theory (DMFT) [39–44]. Recently a DFT + DMFT study to account for both static and dynamic correlations has been carried out to explore this Mott transition and associated compositional phase diagram in Li_xCoO_2 [45]. Here local interactions, which DMFT describes, are seen to strongly impact self energies, occupancies of d orbitals, phase stability, and electronic behavior of LCO at various x . Pristine LCO is an insulator while delithiated phases are moderately correlated Fermi liquids with modest quasiparticle weights. DFT+DMFT also correctly captures the phase stability of LCO as a function of x , without a strong tendency for charge disproportionation at $x = 0.5$ as seen in experiments and unlike what is found in DFT+U [45]. Quasiparticles like polarons are known to affect charge conductivity in batteries [46,47]. It is likely that similar treatment of strong correlations is essential for modeling plausible phase transitions in LMO.

One of the main bottlenecks to the use of DMFT in battery cathodes is that they need to be studied at different states-of-charge. This means dealing with multiple inequivalent sites, and hence solving multi-impurity problems. This has the disadvantage of having to solve very large density matrices, which are not only very expensive, but may often have large off diagonal terms, leading to Fermionic sign problems.

In this paper we predict using DFT+DMFT the phase transitions in layered monoclinic Li_xMnO_2 , as a function of x , and explore the temperature versus x phase diagram. We develop a computationally tractable method to deal with multi-impurity DMFT calculations avoiding Fermionic sign problem and showing excellent match in physical results with conventional multi-impurity DMFT. The electronic and magnetic state of pristine LMO are examined and compared to experimental results at temperatures below and above T_N . The system is then delithiated systematically and for each x we present the spectral functions, magnetic properties, and transition temperatures. We find a metal-insulator Mott transition as a function of delithiation and the emergence of exotic states like ferromagnetic correlated metals with large quasiparticle peaks and charge-ordered ferromagnetic correlated metals with large quasiparticle peaks. We also observe a coherent (Fermi liquid type) to incoherent (non-Fermi liquid type) behavior shown by the system on delithiation as a function of state-of-charge. We observe that the charge disproportionated mixed valence states arises in cases with different quasiparticle peaks at different sites, and postulate this ordering to be present for a range of x . The pathways leading to structural transformations to spinel structure may be traced back to such charge disproportionated state.

II. COMPUTATIONAL METHODOLOGY

A. DFT calculations

Our DFT calculations for structural relaxation were carried out in a plane-wave basis with projector-augmented wave (PAW) potentials [48] as implemented in the Vienna *Ab initio* Simulation Package (VASP) [49,50]. In all our DFT relaxation calculations, we chose as exchange-correlation functional the generalized gradient approximation (GGA), implemented following the Perdew-Burke-Ernzerhof (PBEsol) prescription for solids [51]. The effect of static correlations at the level of DFT was included through the DFT+U formalism and were carried out in the form of GGA+U. The value of U at the Mn sites in the GGA+U scheme was varied between 4.5 and 7.5 eV, with Hund's exchange J_H of 0.5–0.75 eV. For ionic relaxations using the VASP package, internal positions of the atoms were allowed to relax until the forces became less than 0.005 eV/Å. An energy cutoff of 550 eV and a $6 \times 12 \times 4$ Monkhorst-Pack k -points mesh provided good convergence of the total energy. For our DFT+DMFT calculations we are using the full-potential augmented plane-wave basis as implemented in the WIEN2K code package [52]. For the WIEN2K calculations, we used the largest possible muffin-tin radii, and the basis set plane-wave cutoff was defined by $R_{\min} \cdot K_{\max} = 7.5$, where R_{\min} is the muffin-tin radius of the O atoms. The consistency between the VASP and WIEN2K results has always been cross checked.

B. DMFT calculations

DMFT calculations were performed using the TRIQS/DFTTools package [53–55] based on the TRIQS libraries [56]. We perform DMFT calculations in a basis set of maximally localized Wannier functions (MLWF) Wannierized using Wannier90 [57] and the wien2wannier [58] interface. Projective Wannier functions as implemented in the dmftproj module of TRIQS were employed to cross check the results and also to calculate the initial occupancy of the correlated orbitals. The DMFT calculations in both MLWF and projective Wannier functions basis have been found to yield consistent results. All five Mn d orbitals have been taken into account in the correlated subspace. A projection window of -2 eV to $+3$ eV was chosen. The Anderson impurity model constructed by mapping the many-body lattice problem to a local problem of an impurity interacting with a bath was solved using the continuous-time quantum Monte Carlo algorithm in the hybridization expansion (CT-HYB) [59] as implemented in the TRIQS/CTHYB package [60]. For each DMFT step 125 000 cycles of warmup steps and 1 250 000 cycles of measures were performed for the quantum Monte Carlo calculations. We performed one-shot DFT+DMFT calculations, using a fully localized limit (FLL) type double-counting correction [44]. We use a fully rotationally-invariant Kanamori Hamiltonian parametrised by Hubbard U and Hund's coupling J_H , where we set the intraorbital interaction to $U' = U - 2J_H$. For our DMFT calculations we used U values ranging from 4.5 to 7.5 eV and $J_H = 0.5 - 0.75$ eV. The choice of interaction parameters is motivated by previous DMFT study on manganite compounds such as LaMnO_3 , where Mn is in isoelectronic state to

LiMnO₂ and showing a very similar JT distorted crystal structure [61–65]. Real-frequency spectra have been obtained using the maximum-entropy method of analytic continuation as implemented in the TRIQS/MAXENT application [66].

We develop a method to carry out multi-impurity DMFT calculations by mapping multi-impurity problems to equivalent number of single-impurity problems interacting through bath hybridization by means of Wannier projections. Delithiating the system results in formation of crystallographically inequivalent Mn sites in the LMO supercell, which requires solving multi-impurity problems, involving solution of extremely large density matrices, which is computationally expensive, and has Fermionic sign problem at low temperatures. To make the problem tractable, maximally localized Wannier functions (MLWF) were constructed for all structurally inequivalent sites; however, each inequivalent site was solved as a single-impurity problem interacting through the bath with the other inequivalent sites by virtue of the constructed MWLF, and the bath hybridization. In conventional multiple impurity DMFT solving a multi-impurity problem is done by solving all the impurity problems in one go. We, however, solve for the self energy of each impurity problem separately but putting the self energy of all other impurities to 0. Our method solves each Anderson impurity problem separately for the full basis of Wannier functions of all impurities. This method works well for strongly localized systems and makes accurate calculations at low-temperatures converge faster with much less noise, avoiding the Fermionic sign problem. Further details on comparison to conventional DMFT are in the Appendix.

III. RESULTS

A. DFT calculations and construction of Wannier functions

Layered LMO crystallizes in space group $C_{2/m}$, with (experimental) lattice constants $a = 5.438 \text{ \AA}$, $b = 2.808 \text{ \AA}$, $c = 5.387 \text{ \AA}$, with $\alpha = \gamma = 90^\circ$, $\beta = 116^\circ$. It has been synthesized experimentally [3,22,67] although is a metastable compound. We fully geometry optimize the structure using the PBESol functional, with static correlations included at the level of DFT+U, as implemented in the VASP (5.4) plane-wave DFT package, to reduce the external pressure below 0.01 eV/\AA^2 as well as the forces below 0.001 eV/\AA on the ionic positions, and obtain $a = 5.426 \text{ \AA}$. A $3 \times 1 \times 1$ supercell of LMO is shown in Fig. 1(a). The nonspin polarized orbital- and site-resolved DFT band structure, obtained from VASP, is shown in Fig. 1(b), where a metallic ground state is obtained and the Mn d orbitals are seen to cross the Fermi energy. For constructing the orbital-resolved band structure the charge densities are projected onto spherical harmonics. The red bands represent Mn d orbitals while the green bands represent O p orbitals. From the band structure it is also seen that the Mn d orbitals are split into t_{2g} and e_g orbitals due to the octahedral crystal-field splitting. The degeneracy in the Mn e_g orbitals is further broken due to a strong collinear Jahn-Teller distortion. Mn t_{2g} orbitals are also further split into a_{1g} and e_g^π orbitals due to the almost trigonal distortion in the structure. Most importantly it can be inferred from the band structure that a d only model for Wannier projections is sufficient to

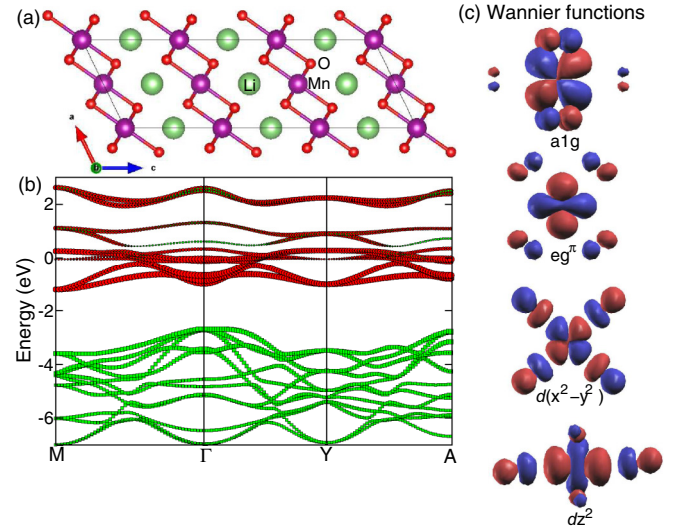


FIG. 1. The crystal structure and associated DFT electronic band-structure and Wannier functions of monoclinic LMO. (a) The crystal structure, (b) the DFT nonmagnetic band structure where the Fermi level is set to 0 eV, and (c) the Wannier orbitals $d_{xz} = a_{1g}$, e_g^π , and $e_g^\sigma = d_{x^2-y^2}$, d_{z^2} . We see well separated Mn d and O p bands and a d model to be sufficient to describe the system, with p contributions accounted for on the tails of the Wannier functions.

describe the correlated Mn d orbitals in the system, since the Mn d and O p bands are well separated in energy. Maximally localized Wannier functions are constructed for the full d manifold of Mn, to allow for high-spin states of Mn. We find the crystal field splitting $\sim 0.48 \text{ eV}$ from Wannier on-site energy calculation. On-site energy difference between Mn t_{2g} and O p states $\sim 3 \text{ eV}$. A d only model is sufficient in this case, as in case of other manganites with similar JT distortions and similar occupancy [68–71]. Any hybridization Mn d and O p is taken into account by the Wannier functions, whereby the O p contributions are considered within the downfolded Mn d orbitals. The Wannier functions for Mn a_{1g} , e_g^π and the two e_g^σ orbitals are shown in Fig. 1(c). The e_g^π orbitals have a much higher spread in space as expected compared to a_{1g} orbitals due to symmetry of the e_g^π bonding. The e_g^σ orbitals show large σ -bonded contributions from O p on tails of the Mn-centered Wannier functions.

B. Single-impurity DMFT calculation

To correctly account for dynamic correlation effects on Mn d states, we first carry out single-impurity DMFT calculations for Mn d based low-energy Hamiltonians defined in the basis of DFT-derived Wannier functions (see Fig. 1).

The paramagnetic state of pristine layered monoclinic LMO at $T = 580 \text{ K}$ shown by the paramagnetic spectral function in Fig. 2(a) (right) displays good agreement with experimental studies [72]. Pristine LMO is an insulator [22,73]; however, experimental value of the electronic band gap is unknown. A wide range of band gap values from 0.3 eV to 1.8 eV have been reported from *ab initio* calculations based on various choices of static Hubbard U in DFT+U calculations [73–77]. We report a paramagnetic band gap of $\sim 0.6 \text{ eV}$, with $U' = 5 \text{ eV}$. We find three slightly degeneracy broken t_{2g}

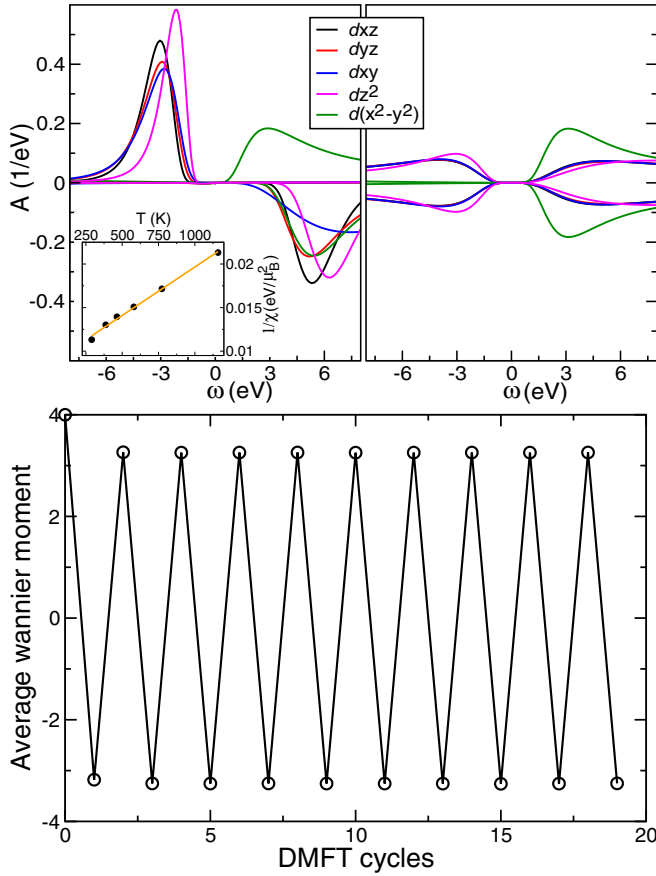


FIG. 2. The DMFT spectral functions and magnetic calculations in LMO. Figure shows the DMFT spectral functions for both single-site spin-polarized (at $T = 58$ K, left panel) and paramagnetic (at $T = 580$ K, right panel) calculations. Inset in left panel shows the plot of $1/\chi$ vs temperature on application of small magnetic fields at various temperatures. The straight line Curie-Weiss fit $\chi = C/(T-\theta)$ for the data is shown.

states that are half-filled, one e_g state is half-filled and one e_g state completely empty. The impurity charge on Mn is 3.99 $|e|$ indicating Mn is in a d^4 (+3) formal oxidation state, again in agreement with XPS experiments [72].

Next, we proceed to explore the magnetism within single-impurity DMFT. For this purpose, we start from the paramagnetic solutions, add a symmetry breaking term in form of a spin-splitting term in the real part of the self energies, and let the DMFT iterative cycle converge to a possible symmetry-broken solution with net-ordered magnetic moment. We carry out the calculations at various different values of inverse temperature with β between 20 and 300 eV^{-1} , where $\beta = \frac{1}{k_B T}$, where k_B is the Boltzmann's constant. At $\beta = 20 \text{ eV}^{-1}$ ($T = 580$ K), the calculations are found to converge to a paramagnetic state, while upon reducing temperature, a transition to a magnetic solution is found. In Fig. 2 (bottom panel) we show a plot of the ordered average Wannier moments of Mn Wannier functions with the number of DMFT iterations. The ordered moments (saturating around $3.25 \mu_B$) are not stable, they oscillate as a function of iteration. The ordered (saturating around $3.25 \mu_B$) Wannier moments show a oscillating behavior as shown in

Fig. 2, meaning that their sign changes from one iteration to the next. This not only rules out a FM-ordered solution within the single-impurity problem, as explained in detail in previous papers [40,78,79], but may indicate a propensity towards antiferromagnetic behavior. The reason for these oscillations is that antiferromagnetism naturally gives rise to two distinct sublattices A and B , with the symmetry for the local Green's functions $G_{A,\sigma}(i\omega_n) = G_{B,\bar{\sigma}}(i\omega_n)$ [40,79]. Here, in our ferromagnetic setup, we do not have a sublattice structure, which corresponds to $G_{A,\sigma}(i\omega_n) = G_{B,\sigma}(i\omega_n)$. Since the impurity hybridization function for sublattice A is calculated from the self-energy and Green's function on sublattice B , it is clear that this leads to oscillations, when the sublattice structure and above given symmetry is not explicitly taken into account. The spectral function for the magnetic state shows insulating behavior. The ordered saturation moment and antiferromagnetic behavior is in good agreement with susceptibility experiments [22].

Using a $U' = 5 \text{ eV}$ within DMFT the antiferromagnetic band gap is $\sim 1.2 \text{ eV}$.

In order to determine the Néel temperature (T_N) we carry out susceptibility calculations with an external field applied on the system. We vary the applied field from 0.01 – 0.03 eV in steps of 0.01 eV, and for each value of temperature we obtain the inverse slope of the magnetization versus applied field within the linear regime. Magnetic fields are applied as a split in energy and the value of magnetic field is added to the DFT Hamiltonian. The contribution $-\hbar_{\text{field}} \times \Sigma$ is added to diagonal elements of the Hamiltonian. This gives the inverse of the uniform susceptibility $1/\chi$ vs temperature T , as shown in Fig. 2 (top left panel inset). By fitting the data to Curie-Weiss law $\chi = C/(T-\theta)$, where C is Curie constant, θ is Weiss temperature in the high temperature regime we find $\theta = 769$ K, in excellent agreement with experimentally reported values on two different samples $\theta = 790$ K, 540 K [22], and a calculated value of $\theta = 790$ K [76]. This has been attributed to the stabilization of antiferromagnetic state due to the co-operative JT distortion [76]. The calculated Néel temperature (T_N) ~ 296 K, is also in agreement with experiments [22]. We use the same set of parameters throughout for benchmarking of T_N with experimental data.

C. Multiple impurity DMFT calculations

Next we look at delithiating the pristine LMO by making two supercells of dimensions $3 \times 1 \times 1$ and $3 \times 2 \times 1$. This results in six and 12 symmetry equivalent Mn sites in case of $3 \times 1 \times 1$ and $3 \times 2 \times 1$ respectively. One Li atom is removed sequentially at each stage and various resulting structures are relaxed within DFT+U using the PBEsol exchange-correlation functional. For the sake of brevity we do not enumerate all the structural details here; however, a significant contraction of lattice parameters and lattice volume is seen on delithiation, as also observed in experiments, as well as a reduction in JT distortion in the system is observed. The various fractions of x considered here are $x = 0.92, 0.83, 0.67, 0.50, 0.33, 0.17, 0.08$, and 0.00. However, $x = 0.00$ is an extreme case: Removing all the Li from the structure is not possible experimentally and makes the structure unstable.

TABLE I. Occupancies in units of $|e|$ and Wannier moments in units of μ_B at different impurity sites.

x	Mn ₁		Mn ₂		Mn ₃		Mn ₄	
	Occupancy	Moment	Occupancy	Moment	Occupancy	Moment	Occupancy	Moment
0.83	4.04	−3.93	4.01	3.94	3.94	−3.75	4.02	3.95
0.67	4.10	3.91	3.98	3.87	3.83	3.65	3.07	2.99
0.50	3.89	3.75	3.07	2.99				
0.33	3.07	2.97	3.06	2.98	3.92	3.77	3.07	2.99
0.17	3.06	2.99	3.05	2.98	3.07	2.98	3.05	2.98

In case of delithiation to $x = 0.83$, the six symmetry equivalent Mn atoms in the pristine $3 \times 1 \times 1$ cell are now split by reduction of symmetry into have 4 structurally inequivalent types, Mn₁, Mn₂, Mn₃, and Mn₄ each with multiplicity 2, 1, 2, and 1 respectively. We find a ferrimagnetic state in this case since from the DMFT spectral functions and from magnetic moments in Table I we see that Mn₁ with multiplicity = 2 (Mn₃ spectral function is electronically similar to Mn₁) is oppositely oriented to Mn₂ with multiplicity = 1 (Mn₄ spectral function is electronically similar Mn₂), as shown in Fig. 3(a). A large quasiparticle peak is seen at the chemical potential in Mn₁ and Mn₃ indicating a correlated metallic state [44]. The quasiparticle peak may be defined as the sharp peak in the correlated spectral function seen at/around chemical potential in the correlated metallic state representing a

quasiparticle state. The height of this peak in the correlated spectral function determines whether it is a large or a small quasiparticle peak. In this paper we distinguish between small quasiparticle peaks where this height is very small and close to 0 and large quasiparticle peaks where this height is large and finite. Thus these four structurally inequivalent types may thus be primarily be grouped into two categories—one with large quasiparticle and the other with small quasiparticle peaks.

The spectral function for the $x = 0.83$ filling is orbital resolved and shows that the t_{2g} orbitals are partially filled and one of the e_g orbitals is partially filled while the other e_g orbital is empty, as shown in Fig. 3(a). This implies an occupancy of d^4 and a formal oxidation state of +3. The occupancies and Wannier moments are given in Table 1. The paramagnetic phase at $T = 580$ K corresponds to a strongly correlated paramagnetic metal with a large quasiparticle peak and non-Fermi liquid behavior as seen from the paramagnetic spectral function shown in the top right panel of Fig. 3(a). The electronic structure for the case of $x = 0.92$ is found to be very similar to $x = 0.83$. For this case of very low state-of-charge we remove one Li from a $3 \times 2 \times 1$ supercell of LMO. Thus there are 11 Li out of 12 and a corresponding fraction of $x = 0.92$. We have six structurally inequivalent sites in this case. The moments indicate a ferrimagnetic arrangement and a correlated metallic electronic state. We do not show the spectral functions here for the sake of brevity.

Delithiated states with $x = 0.67, 0.50, 0.33$ show similar electronic structure to each other across this range of x with certain slight differences, and belong to the same phase of charge-disproportionated ferromagnetic correlated metallic states. In case of $x = 0.67$ and $x = 0.33$, the six symmetry equivalent Mn atoms in the pristine $3 \times 1 \times 1$ cell are again split by reduction of symmetry into four structurally inequivalent types, Mn₁, Mn₂, Mn₃, and Mn₄, each with different multiplicities of 2, 1, 2, 1 respectively; however, in case of $x = 0.50$ there are two structurally inequivalent sites each with multiplicity 3. These sites may primarily be grouped again into two categories—one group with large quasiparticle and the other group with small quasiparticle peaks. The $x = 0.67$ state is ferromagnetic since all Mn sites have the same orientation in the spectral function, as shown in Fig. 3(b), and can also be seen from Moments in Table I. A large quasiparticle peak is seen at the chemical potential in Mn₁ (multiplicity = 2), Mn₃ (multiplicity = 2), and Mn₄ (multiplicity = 1). Mn₃ and Mn₄ are not shown here for the sake of brevity. The middle right panel of Fig. 3 shows the paramagnetic spectral function as a strongly correlated metal for Mn₁, for the case of $x = 0.67$. Large quasiparticle peaks are also seen on Mn₁, with multiplicity of 3 (for $x = 0.50$) and on Mn₁ with

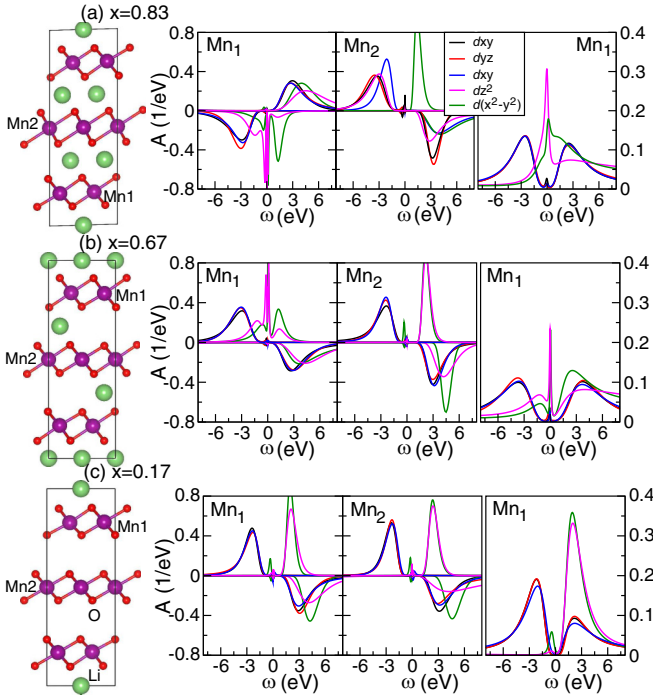


FIG. 3. The structures and orbital-resolved DMFT spectral functions for various states of charge showing the various phases as a function of x . The orbital spectral functions are denoted by the same colors as in Fig. 1. (a) shows the case of $x = 0.83$. The top far-right panel shows the paramagnetic spectral function for Mn₁. (b) shows the case of $x = 0.67$. The middle far-right panel shows the paramagnetic spectral function for Mn₁. (c) shows the case for $x = 0.17$. The bottom far-right panel shows the paramagnetic spectral function of Mn₁.

multiplicity 2 for $x = 0.33$, indicating a strongly-correlated metallic state in all cases. From Table I a mix of +3 and +4 states are seen in all these cases of $x = 0.67, 0.50$, and 0.33 with different fractions of +3 and +4 Mn being present in the system. It is also seen from the spectral functions that this mixed oxidation state and corresponding charge disproportionation may be correlated to different quasiparticle peak heights on different sites. Spectral functions obtained for $x = 0.50$, and 0.33 are seen to be qualitatively similar to the case of $x = 0.67$.

In case of the delithiated state with $x = 0.17$ the six symmetry equivalent Mn atoms in the pristine $3 \times 1 \times 1$ cell are also split by reduction of symmetry into four structurally inequivalent types, Mn_1 , Mn_2 , Mn_3 , and Mn_4 each with multiplicity 2, 1, 2, and 1 respectively. Qualitatively all Mn have similar electronic structures at all sites. A ferromagnetic arrangement is observed here since all Mn sites have same orientation as can be seen from the spectral function in Fig. 3(c) as well as in Table I. A small quasiparticle peak is seen at the chemical potential in each of Mn_1 , Mn_2 , and Mn_3 indicating a moderately correlated metallic state. A majority of +4 oxidation states are seen. There is no charge disproportionation in this case. The bottom-right panel of Fig. 3(c) shows the paramagnetic weakly correlated metallic state with a small quasiparticle peak. To explore a very high state-of-charge we return to the large $3 \times 2 \times 1$ supercell and remove 11 Li out of 12 and explore the high-charge state of $x = 0.08$. In this case there are six structurally inequivalent Mn atoms, each with multiplicity 2, 2, 1, 1, 4, and 2 respectively. When solved we obtain occupancies $Mn_1 = 3.08$, $Mn_2 = 3.08$, $Mn_3 = 3.06$, $Mn_4 = 3.06$, $Mn_5 = 3.04$, $Mn_6 = 3.04$. and moments $Mn_1 = 2.98$, $Mn_2 = 2.97$, $Mn_3 = 2.96$, $Mn_4 = 2.97$, $Mn_5 = 2.98$, $Mn_6 = 2.98$. This indicates a ferromagnetic arrangement again. The spectral function shows a correlated metal with very small quasiparticle peak. We do not show the very similar spectral functions here for the sake of brevity. Fully delithiating the system to $x = 0.0$ results in an unstable structure of MnO_2 (cf. Appendix).

To check the stability of the quasiparticle peaks we carried out calculations varying the values of U from 4.5–7.5 eV, which may be considered a reasonable range of values for Mn d orbitals. We also varied the value of J_H from 0.5 eV to 0.75 eV. On increasing the U to 7.5 eV, we still found the quasiparticle peaks to survive, showing that the large quasiparticle state is a robust state. There is a tendency of smaller J_H to favor antiferromagnetism while larger J_H to favor ferromagnetism. Within reasonable values of Hund's coupling for a $3d$ element like Mn in our case we see that the same J_H , which favors antiferromagnetism in pristine system gives rise to ferromagnetism for $x < 0.67$, with a phase of ferrimagnetism in between at $x = 0.83$.

IV. DISCUSSION

The exotic phase diagram and associated phase transitions in Li_xMnO_2 as a function of x versus temperature, is shown in Fig. 4. The y axis shows the phase change from magnetic to paramagnetic states at each x driven by competition of thermal fluctuations with magnetic order. The change of magnetic phases along x is more nuanced. JT distorted materials show

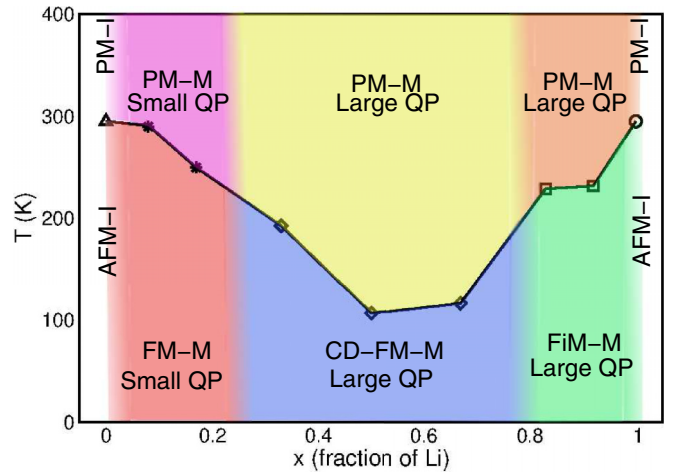


FIG. 4. The different phases at different temperatures of Li_xMnO_2 as a function of Li content. AFM-I refers to antiferromagnetic insulator; FiM-M, ferrimagnetic metal; FM-M, ferromagnetic metal; PM-I, paramagnetic insulator; PM-M, paramagnetic metal; CD, charge disproportionated; and QP, quasiparticle. The different symbols on the line corresponds to the actual data points demarcating the different phases.

large superexchange, which favors antiferromagnetism. This is the case of the pristine material $x = 1$, which is a JT driven antiferromagnetic insulator. As the system is delithiated, JT distortion reduces on different MnO_6 octahedra, which in turn indicates a reduction in monoclinicity. This reduction in JT favors ferromagnetism instead of antiferromagnetism. At $x = 0.83$ there are few sites with reduced JT distortion and hence ferromagnetic exchange whereas majority of other sites still have significant JT distortion and hence show Mn-Mn antiferromagnetic superexchange, leading to an overall ferrimagnetic state. When further delithiated to $x = 0.67$, and beyond, the overall reduction of JT distortion now favors FM double exchange, between different occupancies at majority of Mn sites. Reduction in JT distortion is usually associated with ferromagnetism particularly in manganites [61,62,80]. Charge disproportionation into Mn^{3+}/Mn^{4+} states may be correlated to large quasiparticle peak heights on some sites and small quasiparticle peak heights on others. This charge disproportionation leads to a double exchange mechanism instead of a superexchange.

We next examine the phenomena of a crossover from coherent (Fermi liquid) to incoherent (non-Fermi liquid) behavior as a function of x . We plot $-\text{Im}\Sigma(\omega \rightarrow 0)$, Σ is self energy, as a function of x shown in Fig. 5, which gives the measure of the coherence/incoherence behavior of the correlated metallic states [78,81,82]. A large finite nonzero value of this quantity indicates inelastic electron-electron scattering, leading to finite quasiparticle lifetimes. If the scattering becomes strong (larger than the energy scale given by temperature, for instance), we have incoherent electronic states. Eventually, large electron-electron scattering can induce non-Fermi liquid states [81,82]. Hence a finite nonzero value of $-\text{Im}\Sigma(\omega \rightarrow 0)$ has previously been shown to be correlated to incoherent scattering behavior [78], which has been shown to be indicative of non-Fermi liquid behavior by Dasari *et al.* [81]. Here we observe as shown in Fig. 5 that there is

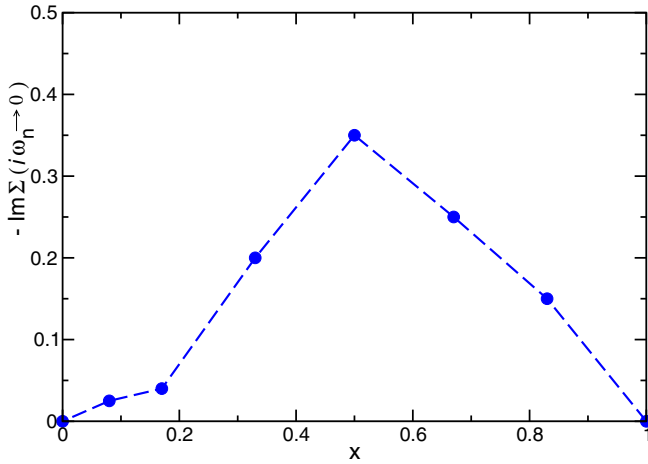


FIG. 5. Plot of $-\text{Im } \Sigma(\omega \rightarrow 0)$, which gives a measure of coherence/incoherence behavior as a function of state-of-charge. A finite nonzero value of this quantity indicates an incoherent scattering behavior. An infinitesimally small value tends to indicate a coherent behavior [78,81].

an increase of incoherent (or non-Fermi liquid-like) behavior with delithiation from $x = 0.83$ to $x = 0.33$. We thus observe a crossover from a coherent (Fermi liquid-type) to incoherent (non-Fermi liquid-type) state on delithiation as a function of state-of-charge and then back to coherent behavior at high states of charge.

To explore the effect of distribution of Li on the charge disproportionated states we carried out DMFT calculations for a different configuration for $x = 0.5$ having a different distribution of Li atoms. We get qualitatively similar physical results. We end up with six different inequivalent sites. Out of these we get a charge disproportionated state with two sites having impurity charge ~ 4 and four sites having impurity charge ~ 3 . This shows that although the method employed is qualitatively very robust, the distribution of charge disproportionated sites do indeed depend on the distribution of Li atoms locally, with the overall result being the same—a charge disproportionated state of $+3/+4$ Mn sites, with a corresponding spin disproportionation. It is to be noted here that the charge disproportionated state with equal number of $+3/+4$ Mn sites (three each) has a lower ground-state energy at the level of DFT calculations.

V. CONCLUSIONS

In summary we have shown the exotic phase diagram and phase transitions in Li_xMnO_2 as a function of state-of-charge x , and temperature. Our study shows a different method of carrying out multi-impurity DMFT calculations in cathode materials in a computationally tractable way, thus opening up the field of battery physics in terms of strong correlations based many-body studies. It demonstrates an electrochemical method of tuning strongly correlated phase transitions and also shows emergence of quasiparticle states, which contribute to charge disproportionation and which eventually lead to structural transformations seen in this material, and helps us in understanding degradation in cathodes.

We find that an antiferromagnetic insulating state emerges in LiMnO_2 , with a Weiss temperature of $\theta = 769$ K, in its $+3$ formal oxidation state, in high-spin configuration, in excellent agreement with experimental measurements. As the system is delithiated at fractions of $x = 0.92$, and 0.83 we predict a ferrimagnetic correlated metallic state thus observing a metal-insulator transition, similar to that in LCO. From the DMFT spectral function this metal-insulator transition is seen to be of a Mott-type transition with a large quasiparticle peak in the strongly correlated metallic state.

At fractions of $x = 0.67$, 0.5 , and 0.33 we find the system to be in ferromagnetic strongly correlated metallic state with a mix of $+3/+4$ formal oxidation states. The pathways leading to the structural transformation to low-energy spinel structure, originates with orderings of $\text{Li}^+/\text{Li}_{\text{vac}}$ and $\text{Mn}^{3+}/\text{Mn}^{4+}$ mixed oxidation states at $x = 0.50$ [9]. It is observed that this $\text{Mn}^{3+}/\text{Mn}^{4+}$ charge disproportionation may be correlated to the different quasiparticle peak heights at different sites. At a high state-of-charge with $x = 0.17$, we find a ferromagnetic correlated metal with a small quasiparticle peak near a formal oxidation state of $+4$. An overall nominal oxidation state change of Mn from $+3$ in LiMnO_2 to $+4$ in MnO_2 is observed, through stages of mixed oxidation states. In all these cases the high-spin state emerges as the most likely state considering the full d manifold of Mn in the model. A crossover from a coherent to incoherent behavior on delithiation as a function of state-of-charge and then back to coherent behavior at high states of charge is observed. Our computationally tractable method of carrying out multi-impurity DMFT calculations involves calculating Wannier projections for all impurities and solving each separately keeping others in the bath, interacting through the bath hybridization, avoiding Fermionic sign problem and matching well with conventional DMFT.

To the best of our knowledge a systematic examination of the electrochemically driven Mott transition and the full phase diagram of LMO from a correlations based perspective does not exist, nor does an explanation for the observed orbital ordering at $x = 0.50$ and our study is expected to give rise to further experimental studies exploring these aspects of this very important cathode material through possible *in situ* XPS+BIS spectra and magnetic susceptibility measurements while charging and discharging of the LMO cathodes. It is also to be noted that without many-body methods like DMFT it is not possible within DFT or DFT+U methods to capture this rich quasiparticle-based physics at moderate values of U , which dominates the physics of battery cathodes on charging-discharging processes both at high- (paramagnetic) and low- (magnetically ordered) temperature regimes.

ACKNOWLEDGMENTS

The authors acknowledge fruitful discussion with Markus Aichhorn and Annalena R. Genreith-Schriever. This work has been funded by the Faraday Institution Degradation Project (FIRG001, FIRG024). Calculations have been performed on the Odyssey Cluster, the CSD3 Cluster of the University of Cambridge. Generous computing resources were provided by the Sulis HPC service (EP/T022108/1), and networking support by CCP-NC (EP/T026642/1), CCP9 (EP/T026375/1), and UKCP (EP/P022561/1).

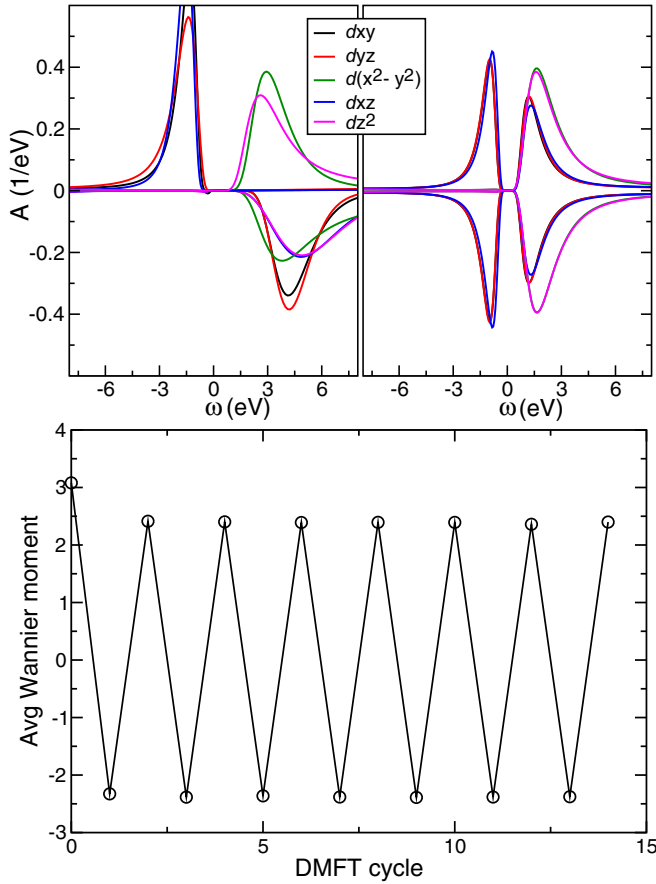


FIG. 6. Figure showing electronic structure of MnO_2 . Top left panel shows DMFT spectral functions at $T = 58$ K, and top right panel shows DMFT spectral function in the paramagnetic phase at $T = 580$ K. The low temperature magnetic phase has oscillating moments as shown in the lower panel and may indicate a propensity towards antiferromagnetic behavior.

APPENDIX

1. DMFT calculations on MnO_2

Although it is nearly impossible to fully delithiate the system experimentally since the resulting MnO_2 structure is unstable, we can theoretically explore this system by constructing a fully delithiated structure, which would albeit be unstable. We construct this structure by removing all Li from pristine LMO. This results in a single inequivalent site and hence a single-impurity problem in DMFT. This system has an impurity charge = 2.98 with three half filled t_{2g} orbitals, two

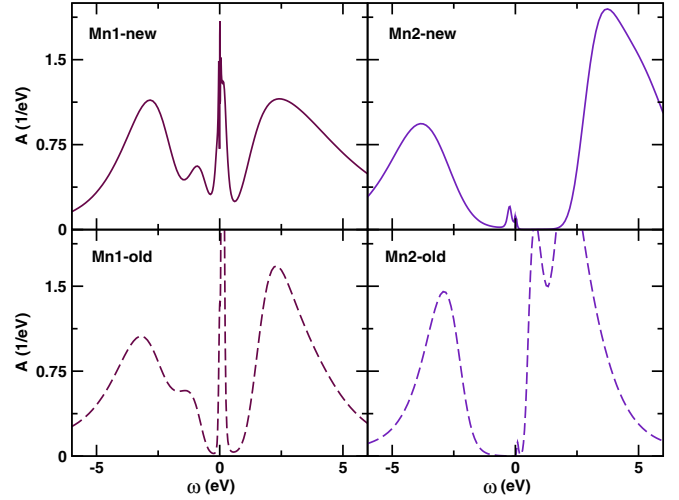


FIG. 7. Figure showing a comparison of spectral functions obtained from our method of multi impurity DMFT calculation with that obtained from conventional multi impurity DMFT calculations for the case of $x = 0.5$, with 2 structurally inequivalent impurity sites.

empty e_g orbitals. The average Wannier moments fluctuates with a maximum saturation value of $\sim 2.50\mu_B$. This indicates presence of antiferromagnetic fluctuations in the system. The system is insulating as seen from spectral functions shown in Fig. 6.

2. Comparison of our DMFT method with conventional DMFT

To check the validity and robustness of our method against conventional multi impurity DMFT calculations we carried out conventional two impurity DMFT calculations for $x = 0.5$. This shows the same charge disproportionation and ferromagnetic behavior at low temperature, and very similar spectral functions for paramagnetic phase as well, as shown in Fig. 7, that our method has an excellent match with the conventional way of calculating multi-impurity problems in DMFT. The minor differences in spectral functions may be attributed to the extra effect of localization in our approximation; however, we see that all the qualitative features are very well reproduced by our method. In terms of charges and magnetic moments, for low-temperature magnetic phase, the conventional DMFT multi-impurity calculation gives charges of $3.97e$ and $3.01e$ for Mn_1 and Mn_2 respectively and Wannier moments of 3.86 and 2.75 . This can be easily compared to the occupancy and Wannier moments of Mn_1 and Mn_2 for our method from Table I and we see that there is very little to no difference in qualitative results between the two methods.

- [1] A. R. Armstrong and P. G. Bruce, *Nature (London)* **381**, 499 (1996).
- [2] F. Capitaine, P. Gravereau, and C. Delmas, *Solid State Ion.* **89**, 197 (1996).
- [3] G. Vitins and K. West, *J. Electrochem. Soc.* **144**, 2587 (1997).

- [4] M. Thackeray, W. David, P. Bruce, and J. Goodenough, *Mater. Res. Bull.* **18**, 461 (1983).
- [5] M. Thackeray, P. Johnson, L. de Picciotto, P. Bruce, and J. Goodenough, *Mater. Res. Bull.* **19**, 179 (1984).
- [6] M. M. Thackeray, S.-H. Kang, C. S. Johnson, J. T. Vaughey, R. Benedek, and S. A. Hackney, *J. Mater. Chem.* **17**, 3112 (2007).

- [7] M. Freire, N. V. Kosova, C. Jordy, D. Chateigner, O. I. Lebedev, A. Maignan, and V. Pralong, *Nat. Mater.* **15**, 173 (2016).
- [8] A. Chakraborty, S. Kunikuruvan, S. Kumar, B. Markovsky, D. Aurbach, M. Dixit, and D. T. Major, *Chem. Mater.* **32**, 915 (2020).
- [9] I. D. Seymour, S. Chakraborty, D. S. Middlemiss, D. J. Wales, and C. P. Grey, *Chem. Mater.* **27**, 5550 (2015).
- [10] I. D. Seymour, D. J. Wales, and C. P. Grey, *J. Phys. Chem. C* **120**, 19521 (2016).
- [11] Y. Zhang, H. Xie, H. Jin, Q. Zhang, Y. Li, X. Li, K. Li, and C. Bao, *IOP Conf. Ser.: Earth Environ. Sci.* **603**, 012051 (2020).
- [12] J. Greedan, N. Raju, and I. Davidson, *J. Solid State Chem.* **128**, 209 (1997).
- [13] T. Ohzuku, A. Ueda, and M. Nagayama, *J. Electrochem. Soc.* **140**, 1862 (1993).
- [14] J. R. Dahn, U. von Sacken, M. W. Juskow, and H. Al-Janaby, *J. Electrochem. Soc.* **138**, 2207 (1991).
- [15] M. Broussely, F. Pertion, P. Biensan, J. Bodet, J. Labat, A. Lecerf, C. Delmas, A. Rougier, and J. Pérès, *J. Power Sources* **54**, 109 (1995).
- [16] T. Ohzuku and Y. Makimura, *Chem. Lett.* **30**, 642 (2001).
- [17] N. Yabuuchi and T. Ohzuku, *J. Power Sources* **119-121**, 171 (2003).
- [18] C. Xu, K. Märker, J. Lee, A. Mahadevegowda, P. J. Reeves, S. J. Day, M. F. Groh, S. P. Emge, C. Ducati, B. Layla Mehdi *et al.*, *Nat. Mater.* **20**, 84 (2021).
- [19] C. Xu, P. J. Reeves, Q. Jacquet, and C. P. Grey, *Adv. Energy Mater.* **11**, 2003404 (2021).
- [20] C. Julien, A. Mauger, K. Zaghib, and H. Groult, *Materials* **9**, 595 (2016).
- [21] A. K. Stephan, *Joule* **4**, 1632 (2020).
- [22] M. Tabuchi, K. Ado, H. Kobayashi, H. Kageyama, C. Masquelier, A. Kondo, and R. Kanno, *J. Electrochem. Soc.* **145**, L49 (1998).
- [23] Y. Shao-Horn, S. A. Hackney, A. R. Armstrong, P. G. Bruce, R. Gitzendanner, C. S. Johnson, and M. M. Thackeray, *J. Electrochem. Soc.* **146**, 2404 (1999).
- [24] J. Reed, G. Ceder, and A. V. D. Ven, *Electrochem. Solid-State Lett.* **4**, A78 (2001).
- [25] A. R. Armstrong, N. Dupre, A. J. Paterson, C. P. Grey, and P. G. Bruce, *Chem. Mater.* **16**, 3106 (2004).
- [26] S. Kim, X. Ma, S. P. Ong, and G. Ceder, *Phys. Chem. Chem. Phys.* **14**, 15571 (2012).
- [27] J. N. Reimers and J. R. Dahn, *J. Electrochem. Soc.* **139**, 2091 (1992).
- [28] T. Ohzuku and A. Ueda, *J. Electrochem. Soc.* **141**, 2972 (1994).
- [29] G. G. Amatucci, J. M. Tarascon, and L. C. Klein, *J. Electrochem. Soc.* **143**, 1114 (1996).
- [30] M. Ménétrier, I. Saadoun, S. Levasseur, and C. Delmas, *J. Mater. Chem.* **9**, 1135 (1999).
- [31] E. Flores, N. Mozhzhukhina, U. Aschauer, and E. J. Berg, *ACS Appl. Mater. Interfaces* **13**, 22540 (2021).
- [32] A. J. Merryweather, C. Schnedermann, Q. Jacquet, C. P. Grey, and A. Rao, *Nature (London)* **594**, 522 (2021).
- [33] M. D. Radin, S. Hy, M. Sina, C. Fang, H. Liu, J. Vinkeviciute, M. Zhang, M. S. Whittingham, Y. S. Meng, and A. Van der Ven, *Adv. Energy Mater.* **7**, 1602888 (2017).
- [34] P. Werner and A. J. Millis, *Phys. Rev. B* **75**, 085108 (2007).
- [35] A. Liebsch, *Phys. Rev. B* **77**, 115115 (2008).
- [36] E. Gati, U. Tutsch, A. Naji, M. Garst, S. Köhler, H. Schubert, T. Sasaki, and M. Lang, *Crystals* **8**, 38 (2018).
- [37] J. F. Oliveira, M. B. Fontes, M. Moutinho, S. E. Rowley, E. Baggio-Saitovitch, M. B. Silva Neto, and C. Enderlein, *Commun. Mater.* **2**, 1 (2021).
- [38] C. A. Marianetti, G. Kotliar, and G. Ceder, *Nat. Mater.* **3**, 627 (2004).
- [39] A. Georges and G. Kotliar, *Phys. Rev. B* **45**, 6479 (1992).
- [40] A. Georges, G. Kotliar, W. Krauth, and M. J. Rozenberg, *Rev. Mod. Phys.* **68**, 13 (1996).
- [41] D. Vollhardt, *Ann. Phys.* **524**, 1 (2012).
- [42] A. Georges, *AIP Conf. Proc.* **715**, 3 (2004).
- [43] G. Kotliar, S. Y. Savrasov, K. Haule, V. S. Oudovenko, O. Parcollet, and C. A. Marianetti, *Rev. Mod. Phys.* **78**, 865 (2006).
- [44] K. Held, *Adv. Phys.* **56**, 829 (2007).
- [45] E. B. Isaacs and C. A. Marianetti, *Phys. Rev. B* **102**, 045146 (2020).
- [46] W. H. Sio, C. Verdi, S. Poncé, and F. Giustino, *Phys. Rev. B* **99**, 235139 (2019).
- [47] W. H. Sio, C. Verdi, S. Poncé, and F. Giustino, *Phys. Rev. Lett.* **122**, 246403 (2019).
- [48] P. E. Blöchl, *Phys. Rev. B* **50**, 17953 (1994).
- [49] G. Kresse and J. Hafner, *Phys. Rev. B* **47**, 558 (1993).
- [50] G. Kresse and J. Furthmüller, *Phys. Rev. B* **54**, 11169 (1996).
- [51] J. P. Perdew, K. Burke, and M. Ernzerhof, *Phys. Rev. Lett.* **77**, 3865 (1996).
- [52] P. Blaha, K. Schwarz, F. Tran, R. Laskowski, G. K. H. Madsen, and L. D. Marks, *J. Chem. Phys.* **152**, 074101 (2020).
- [53] M. Aichhorn, L. Pourovskii, V. Vildosola, M. Ferrero, O. Parcollet, T. Miyake, A. Georges, and S. Biermann, *Phys. Rev. B* **80**, 085101 (2009).
- [54] M. Aichhorn, L. Pourovskii, and A. Georges, *Phys. Rev. B* **84**, 054529 (2011).
- [55] M. Aichhorn, L. Pourovskii, P. Seth, V. Vildosola, M. Zingl, O. E. Peil, X. Deng, J. Mravlje, G. J. Kraberger, C. Martins *et al.*, *Comput. Phys. Commun.* **204**, 200 (2016).
- [56] O. Parcollet, M. Ferrero, T. Ayrat, H. Hafermann, I. Krivenko, L. Messio, and P. Seth, *Comput. Phys. Commun.* **196**, 398 (2015).
- [57] G. Pizzi, V. Vitale, R. Arita, S. Blügel, F. Freimuth, G. Géranton, M. Gibertini, D. Gresch, C. Johnson, T. Koretsune *et al.*, *J. Phys.: Condens. Matter* **32**, 165902 (2020).
- [58] J. Kuneš, R. Arita, P. Wissgott, A. Toschi, H. Ikeda, and K. Held, *Comput. Phys. Commun.* **181**, 1888 (2010).
- [59] P. Werner and A. J. Millis, *Phys. Rev. B* **74**, 155107 (2006).
- [60] P. Seth, I. Krivenko, M. Ferrero, and O. Parcollet, *Comput. Phys. Commun.* **200**, 274 (2016).
- [61] H. Banerjee, O. Janson, K. Held, and T. Saha-Dasgupta, *Phys. Rev. B* **100**, 115143 (2019).
- [62] H. Banerjee and M. Aichhorn, *Phys. Rev. B* **101**, 241112(R) (2020).
- [63] H. Banerjee, *Mod. Phys. Lett. B* **34**, 2030006 (2020).
- [64] C. A. Marianetti, K. Haule, and O. Parcollet, *Phys. Rev. Lett.* **99**, 246404 (2007).
- [65] P. Wissgott, A. Toschi, H. Usui, K. Kuroki, and K. Held, *Phys. Rev. B* **82**, 201106(R) (2010).
- [66] G. J. Kraberger, R. Triebl, M. Zingl, and M. Aichhorn, *Phys. Rev. B* **96**, 155128 (2017).
- [67] T. Uyama, K. Mukai, and I. Yamada, *RSC Adv.* **8**, 26325 (2018).

- [68] Y.-F. Yang and K. Held, *Phys. Rev. B* **76**, 212401 (2007).
- [69] A. Yamasaki, M. Feldbacher, Y.-F. Yang, O. K. Andersen, and K. Held, *Phys. Rev. Lett.* **96**, 166401 (2006).
- [70] Y.-F. Yang and K. Held, *Phys. Rev. B* **82**, 195109 (2010).
- [71] H. Das, G. Sangiovanni, A. Valli, K. Held, and T. Saha-Dasgupta, *Phys. Rev. Lett.* **107**, 197202 (2011).
- [72] X. Li, Z. Su, and Y. Wang, *J. Alloys Compd.* **735**, 2182 (2018).
- [73] V. Galakhov, M. Korotin, N. Ovechkina, E. Kurmaev, V. Gorshkov, D. Kellerman, S. Bartkowski, and M. Neumann, *Eur. Phys. J. B* **14**, 281 (2000).
- [74] D. J. Singh, *Phys. Rev. B* **55**, 309 (1997).
- [75] N. Nath Shukla and R. Prasad, *J. Phys. Chem. Solids* **67**, 1731 (2006).
- [76] S. K. Mishra and G. Ceder, *Phys. Rev. B* **59**, 6120 (1999).
- [77] M. Tuccillo, O. Palumbo, M. Pavone, A. B. Muñoz-García, A. Paolone, and S. Brutti, *Crystals* **10**, 526 (2020).
- [78] H. Banerjee, H. Schnait, M. Aichhorn, and T. Saha-Dasgupta, *Phys. Rev. B* **105**, 235106 (2022).
- [79] M. Rozenberg, in *Many-Body Methods for Real Materials Modeling and Simulation*, Vol. 9 (Forschungszentrum, Jülich, 2019).
- [80] J. H. Lee, K. T. Delaney, E. Bousquet, N. A. Spaldin, and K. M. Rabe, *Phys. Rev. B* **88**, 174426 (2013).
- [81] N. Dasari, Yamijala S. R. K. C. Sarma, M. Jain, T. S. Dasgupta, J. Moreno, M. Jarrell, and N. S. Vidhyadhiraja, *Phys. Rev. B* **94**, 085143 (2016).
- [82] P. Werner, E. Gull, M. Troyer, and A. J. Millis, *Phys. Rev. Lett.* **101**, 166405 (2008).